ADVANCED MATERIALS
www.advmat.de

Spin–Phonon Coupling in Ferromagnetic Monolayer Chromium Tribromide

Jiangbin Wu, Yu Yao, Miao-Ling Lin, Malte Rösner, Zhonghao Du, Kenji Watanabe, Takashi Taniguchi, Ping-Heng Tan, Stephan Haas,* and Han Wang**

Novel 2D magnets exhibit intrinsic electrically tunable magnetism down to the monolayer limit, which has significant value for nonvolatile memory and emerging computing device applications. In these compounds, spin–phonon coupling (SPC) typically plays a crucial role in magnetic fluctuations, magnon dissipation, and ultimately establishing long-range ferromagnetic order. However, a systematic understanding of SPC in 2D magnets that combines theory and experiment is still lacking. In this work, monolayer chromium tribromide is studied to investigate SPC in 2D magnets via Raman spectroscopy and first principle calculations. The experimental Curie temperature and phonon shifts are found to be in good agreement with the numerical simulations. Specifically, it is demonstrated how magnetic exchange interactions affect phonon vibrations, which helps establish design fundamentals for 2D magnetic materials and other related devices.

1. Introduction

Recently, several magnetic van der Waals monolayer compounds have been successfully identified and explored, including new compounds in the 2D functional quantum materials family, $Cr_2Ge_2Te_6$,[1] CrI_3,[2] $CrBr_3$,[3] and Fe_3GeTe_2.[4] The observed magnetic properties of these compounds indicate dependences on material thickness, pressure, and electrostatic bias.[2,4a,5] Some novel devices, such as multiple-spin-filter magnetic tunnel junctions, have been proposed and shown to have promising applications.[6] Moreover, 2D magnets could greatly advance sensors and nonvolatile memories that require a high data density with a long retention time.[7] In order to engineer the potential of these 2D magnets, it is crucial to investigate their intrinsic spin–phonon coupling (SPC) systematically, which is a key mechanism behind magnetic fluctuations, magnon dissipation, and establishing long-range ferromagnetic.[8]

Lattice dynamics and electronic properties of 2D materials have been widely quantified by Raman spectroscopy.[9] Similar methods can be used to observe SPC in 2D magnets[10] such as FeF_2, $FePS_3$, and $Cr_2Ge_2Te_6$. However, many previous experimental studies have focused on the effects of magnetism on phonon frequencies. Additionally, some theoretical models approximate the interaction between magnons and phonons with localized spin, which has successfully predicted magnon softening[11] and phonon frequency shifts at low temperature.[12] In contrast, there have been a limited number of theoretical studies that examine SPC in 2D magnets,[8h,13] while concentrating on spin-induced phonon shifts. Therefore, a comprehensive study of SPC in 2D magnets is needed to understand the effect of spin and lattice degrees of freedom on the directions and amplitudes of phonon shifts.

We investigated the crystal structure, magnetic exchange interactions, critical temperatures, and phonon properties of

---

J. Wu, Z. Du, H. Wang
Ming Hsieh Department of Electrical and Computer Engineering
University of Southern California
Los Angeles, CA 90089, USA
E-mail: han.wang.4@usc.edu

Y. Yao, S. Haas
Department of Physics & Astronomy
University of Southern California
Los Angeles, CA 90089, USA
E-mail: shaas@usc.edu

M.-L. Lin, P.-H. Tan
State Key Laboratory of Superlattices and Microstructures, Institute of Semiconductors
Chinese Academy of Sciences
Beijing 100083, China
E-mail: phtan@semi.ac.cn

The ORCID identification number(s) for the author(s) of this article can be found under https://doi.org/10.1002/adma.202108506.

DOI: 10.1002/adma.202108506

M. Rösner
Theory of Condensed Matter Department
Radboud University
6500 GL, Nijmegen 29777, Netherlands

K. Watanabe
Research Center for Functional Materials
National Institute for Materials Science
1-1 Namiki, Tsukuba 305-0044, Japan

T. Taniguchi
International Center for Materials Nanoarchitectonics
National Institute for Materials Science
1-1 Namiki, Tsukuba 305-0044, Japan

P.-H. Tan
Center of Materials Science and Optoelectronics Engineering & CAS
Center of Excellence in Topological Quantum Computation
University of Chinese Academy of Sciences
Beijing 100049, China

H. Wang
Mork Family Department of Chemical Engineering and Material Science
University of Southern California
Los Angeles, CA 90089, USA

the ferromagnetic monolayer $CrBr_3$ by combining temperature-dependent Raman spectroscopy and first-principle calculations. The Raman-active phonon frequencies of monolayer $CrBr_3$ show blueshifts below ≈25 K, which we correlate with the magnetic Curie temperature (T_c). The observed effects of SPC on phonon frequency were reproduced using density functional theory (DFT) in conjunction with a finite-displacement approach. The calculated critical temperatures and SPC-induced phonon shifts are found to agree well with the experimental measurements. In conclusion, we found that SPC is predominantly caused by the varying exchange interactions as the atoms oscillate about their equilibrium positions.

2. Results and Discussion

Figure 1a shows a schematic plot of the monolayer $CrBr_3$ crystal structure. The Cr atoms form a honeycomb lattice, which is sandwiched by two atomic planes of Br atoms. The parallelogram in Figure 1a represents a unit cell containing two Cr atoms (blue) and six Br atoms (red). The formally charged Cr^{3+} ions are located at the center of a slightly distorted octahedron formed by Br atoms. Magnetism in $CrBr_3$ originates from the partially filled d shells of the Cr atoms (electronic configuration of $3d^3$). According to ligand field theory, the crystal field, which is combined with halide ligands in an octahedral environment, results in a splitting of the Cr d orbitals into two symmetric classes: A set of triply degenerate t_{2g} orbitals (with lower energy), and a set of doubly degenerate e_g orbitals (with higher energy).[14] The half-occupied Cr t_{2g} orbital yields $S = 3/2$, which creates an atomic magnetic moment of 3 μ_B for each Cr atom. The monolayer $CrBr_3$ is ferromagnetic,[3a,15] which is exfoliated from its bulk material onto a Si/SiO_2 substrate (see Experimental Section for details). An optical image of a monolayer $CrBr_3$ flake is shown in Figure 1b. We used atomic force microscopy to measure the thickness of the monolayers. The resulting atomic force microscopy image is shown in Figure 1c, and the thickness was ≈0.8 nm, which is below the thickness of two-layer spacings, ≈1.2 nm.

Monolayer $CrBr_3$ belongs to the space group D_{3d} and has 8 atoms per unit cell. There are 24 normal vibration modes at the center of the Brillouin zone: $\Gamma = 4E_g + 2A_{1g} + 2A_{2g} + 4E_u + 2A_{1u} + 2A_{2u}$. Here, E_g and E_u are doubly degenerate, and the E_g and A_{1g} modes are Raman active. The Raman tensors (R) of A_{1g} and E_g are $R(A_{1g}) = \begin{bmatrix} a & 0 & 0 \\ 0 & a & 0 \\ 0 & 0 & b \end{bmatrix}$ and $R(E_g) = \begin{bmatrix} c & 0 & 0 \\ 0 & -c & d \\ 0 & d & 0 \end{bmatrix}\begin{bmatrix} 0 & -c & -d \\ -c & 0 & 0 \\ -d & 0 & 0 \end{bmatrix}$, respectively, which means that with parallel polarization (*XX*), both A_{1g} and E_g modes can be observed. However, with cross polarization (*XY*), the A_{1g} modes are silenced, whereas the E_g modes still exhibit the same intensity as that with *XX* polarization. Although the in the ferromagnetic order, there should be imaginary off-diagonal components in the Raman tensor,[16] but these terms can be neglected (see Note S1, Supporting Information, for details). The measured polarized Raman spectra of monolayer $CrBr_3$ are shown in **Figure 2**. The four E_g modes are located at 73.7 cm^{-1} (E_g^1), 142.8 cm^{-1} (E_g^2), 152.6 cm^{-1} (E_g^3), and 283.9 cm^{-1} (E_g^4), and the two A_{1g} modes are at 105.8 cm^{-1} (A_{1g}^1) and 183.8 cm^{-1} (A_{1g}^2). Two laser wavelengths (753 and 594 nm) are used here to observe the E_g^1 and E_g^4 modes. We attribute the varied intensities of these modes excited by different wavelength to the unique symmetry-dependent vibronic coupling in this system, akin to interlayer modes in twisted multilayer graphene.[17]

Figure 3 presents the temperature dependence of the Raman spectra in the A_{1g}^1, E_g^2, E_g^3, and A_{1g}^2 range from 6 to 70 K. The corresponding frequency (Raman shift) of each mode is shown in the lower panel. In common nonmagnetic materials, the temperature-dependent phonon frequency can be described by a model that includes phonon self-energy terms due to three and four phonon anharmonic processes.[18]

$$\omega(T) = A\left(1 + \frac{2}{e^x - 1}\right) + B\left(1 + \frac{3}{e^y - 1} + \frac{3}{\left(e^y - 1\right)^2}\right) \tag{1}$$

where A and B are constants, $x = \hbar\omega_0/2k_BT$, $y = \hbar\omega_0/3k_BT$, and ω_0 is the phonon frequency at 0 K (see Figure S1, Supporting Information, for details). At temperatures above T_c, this model is sufficient for predicting temperature-dependent phonon frequencies.[18] We fit the above anharmonic model with the observed temperature-dependent phonon shifts in monolayer $CrBr_3$ for temperatures above the T_c, as shown in Figure 3. Clearly, when the temperature is lower than 25 K, the anharmonic model is less accurate. Instead, the observed phonon frequencies of each mode show a marked increase

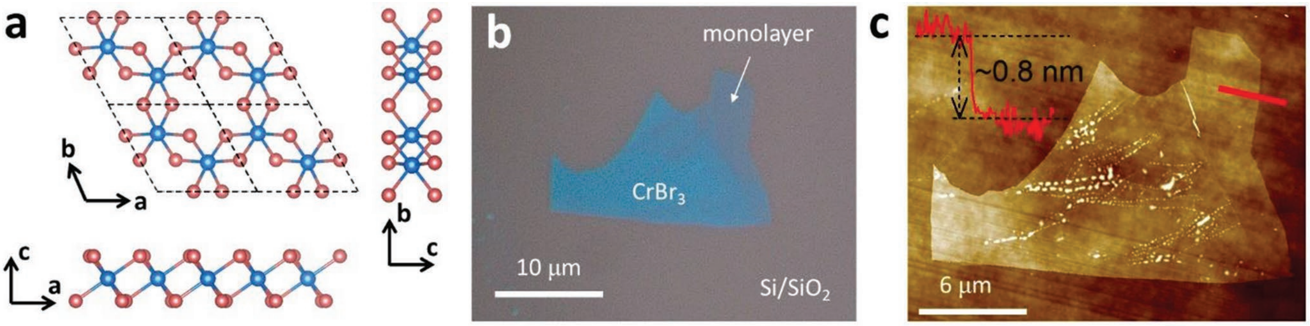

Figure 1. a) Atomic structure of monolayer $CrBr_3$. The unit cell of $CrBr_3$ includes two Cr (blue) and six Br atoms (red). b) Optical images of a $CrBr_3$ flake. The $CrBr_3$ sample was prepared on a Si/SiO_2 substrate. c) Atomic force microscopy image of the $CrBr_3$ flake in (b). Only the upper right corner of the sample is monolayer $CrBr_3$ (shown in the inset as a line-plot).

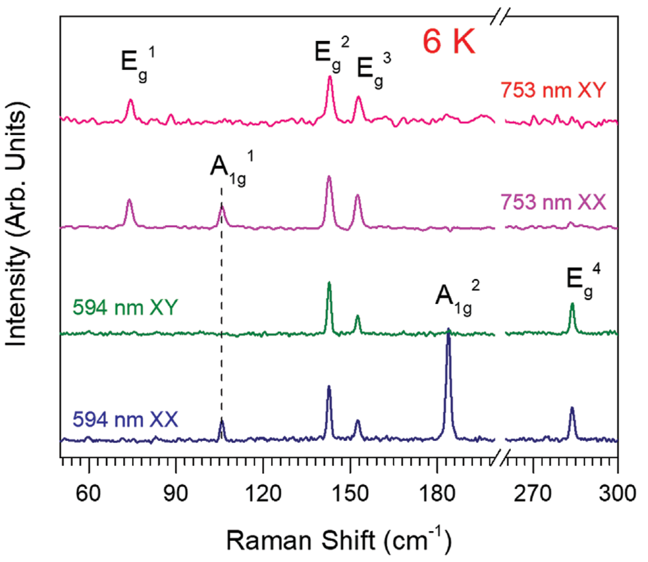

Figure 2. Raman spectra of monolayer $CrBr_3$ at laser wavelengths of 594 and 753 nm and with different polarization configurations (*XX* and *XY*), in the regime of E_g^1, A_{1g}^1, E_g^2, E_g^3, A_{1g}^2, and E_g^4 modes. The spectra are taken at temperature 6 K. The dashed line is a visual aid.

when compared to the nonmagnetic model, which is similar with the temperature-dependent Raman shift in the bulk $CrBr_3$.[19] This is indicative of ferromagnetic phase and SPC in monolayer $CrBr_3$ and the accompanying onset of SPC induced renormalizations. Indeed, the onset temperature of ≈25 K is in good agreement with values of T_c extracted from transport measurements.[20] The blueshifts of phonon frequencies due to the SPC for the A_{1g}^1, E_g^2, E_g^3, and A_{1g}^2 modes are 0.3, 0.33, 0.26, and 0.37 cm^{-1}, respectively, which correspond to 0.28%, 0.23%, 0.17%, and 0.20%, respectively, with respect to their own phonon frequencies.

We notice that the Cr–Br–Cr angle is very close to 90° (95.2° by generalized gradient approximation, GGA). According to the Goodenough–Kanamori–Anderson rule,[21] this signals the existence of a ferromagnetic super-exchange interaction along the Cr–Br–Cr path.[22]The underlying origin of ferromagnetism within single-layer $CrBr_3$ (and other single-layer chromium trihalides) can be qualitatively understood from the competition of direct exchange between the Cr–Cr atoms and the super-exchange between Cr–Cr nearest neighbors, mediated by a central Br atom,[23] which is controlled by effective Coulomb repulsion within the Cr d states. A more-detailed recent report of monolayer CrI_3 shows that the dominant contribution to the exchange interactions between Cr–Cr couples originates from two orbital channels, t_{2g}–t_{2g} and t_{2g}–e_g.[24] Particularly, the antiferromagnetic coupling from the t_{2g}–t_{2g} orbital channel competes with the ferromagnetic coupling from the t_{2g}–e_g orbital channel.

To systematically investigate SPC in monolayer $CrBr_3$ from first principles, we performed GGA+U calculations with varying Hubbard-*U* values. For each Hubbard-*U*, we optimized the lattice structure and calculated the Cr magnetic moments, the strength of exchange interactions, phonon frequencies at Brillouin zone center, and finally the SPC induced phonon frequency shifts. The effective Hubbard-*U* (U_{eff}), $U_{\text{eff}} \approx U - J$, where *J* is the Hund's coupling, varied from 0 to 6. We found that the lattice constant of the ferromagnetic ground state grows linearly with U_{eff}. This is similar to observations in 3D bulk materials[25] (see Figure S2, Supporting Information). On the other hand, the ferromagnetic state itself with about 3 μ_B per Cr atom is found to be independent of the Coulomb interaction. And the total energy of the antiferromagnetic phase is always higher than in the ferromagnetic phase.

In order to further model the magnetic properties of monolayer $CrBr_3$, we utilized a 2D Heisenberg model, with a hexagonal lattice, that describes Cr localized spins. The corresponding spin Hamiltonian can be written as $H = \sum_{\langle i,j\rangle} J_{i,j} S_i S_j + \sum_i D(S_i^z)^2$, where S_i and S_j are the magnetic moments (in μ_B) at sites *i* and *j*, S_i^z is the z component of magnetic moment S_i, $J_{i,j}$ is the exchange interaction between sites *i* and *j*, and *D* is the anisotropy constant. We calculated the exchange interactions between the nearest neighbors $J_1 = -2.57$ meV, second nearest neighbors $J_2 = -0.36$ meV, and third nearest neighbors $J_3 = 0.14$ meV in GGA ($U_{\text{eff}} = 0$ eV), where the negative values of *J* indicate ferromagnetic interactions, and the values of *J* are in line with the results in previous reports.[22,26] The results show that the exchange interactions between the second and third nearest neighbors are sufficiently small compared to the nearest-neighbor interaction in monolayer $CrBr_3$. Thus, we will only focus on the nearest-neighbor exchange interactions in the following. As each Cr site holds a magnetic moment of ≈3 μ_B, J_{NN} can be estimated via

$$J_{\text{NN}} = \frac{E_{\text{FM}} - E_{\text{AFM}}}{6|S|^2} \tag{2}$$

where $|S| = 3/2$. E_{FM} and E_{AFM} are the total electronic energy of one monolayer $CrBr_3$ unit cell with ferromagnetic (FM) and antiferromagnetic (AFM) configurations, respectively.[22] The prefactor 6 comes from the fact that each unit cell contains two Cr atoms, and each Cr atom has three nearest neighbors in the honeycomb lattice. In our calculations, we observe that J_{NN} decreases almost linearly (ferromagnetic interaction getting stronger) as the Hubbard-*U* value increases, as listed in **Table 1**. In monolayer CrI_3, Kashin et al. found a decay of the t_{2g}–t_{2g} exchange interactions for increasing *U* and a nearly constant behavior of the t_{2g}–e_g coupling for $U > 1$ eV, so that the total effective exchange linearly increases with *U*.[24] We expect a similar mechanism in monolayer $CrBr_3$ which explains the almost linear strengthening of J_{NN}.

The anisotropy coefficient *D* can be obtained from the energy difference of the out-of-plane and the in-plane magnetization. Our first-principle computation of the magnetic anisotropy energy indicates that monolayer $CrBr_3$ has an out-of-plane easy axis, which agrees with previous experimental results.[2] With the consideration of spin–orbit coupling (SOC), the exchange coupling and the anisotropy constant are listed in Table 1. The critical temperature of this model can be determined via classical Monte Carlo simulations, yielding[27]

$$T_c = T_c^{\text{Ising}} \tan h^{1/4}\left[\frac{6}{z}\log\left(1 + 0.033\frac{D}{J_{\text{NN}}}\right)\right] \tag{3}$$

where $T_c^{\text{Ising}} = 1.52|S|^2(-J_{\text{NN}})/k_B$. The T_c of monolayer $CrBr_3$ is estimated to be 21.5–29.4 K, depending on the value of U_{eff},

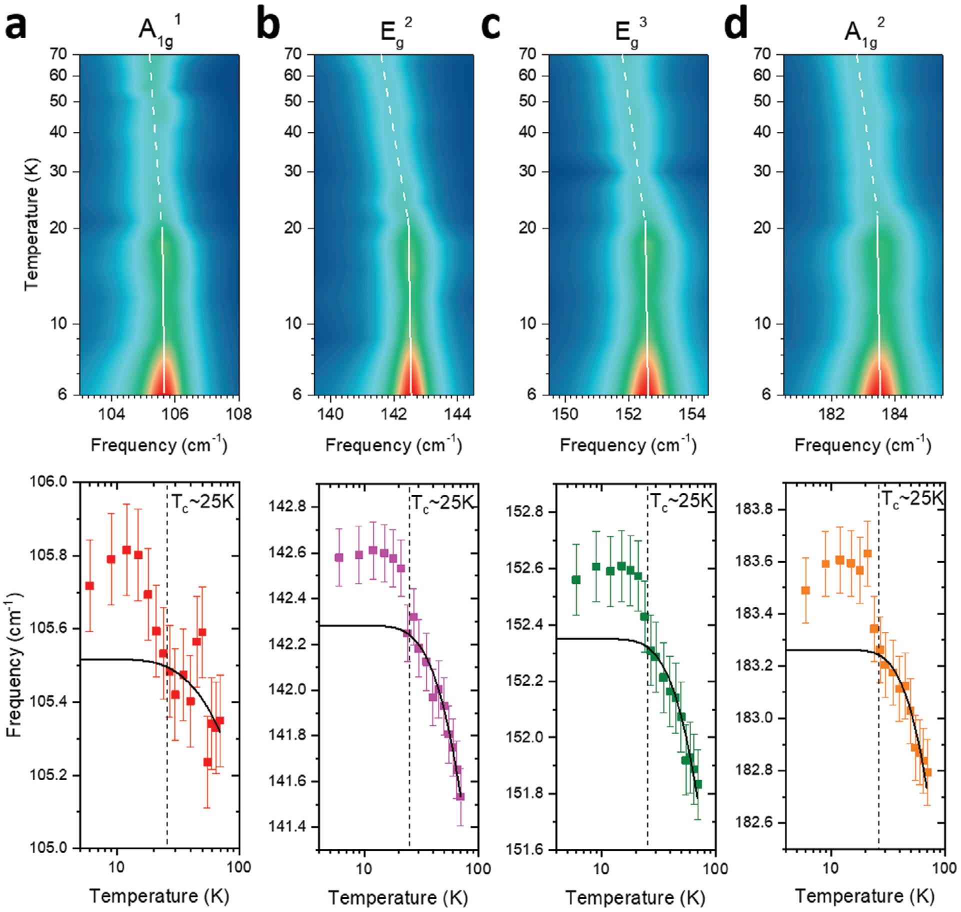

Figure 3. a–d) Temperature-dependent Raman spectra of monolayer $CrBr_3$ in the region of A_{1g}^1 (a), E_g^2 (b), E_g^3 (c), and A_{1g}^2 (d) modes (top) and corresponding temperature-dependent phonon frequencies (bottom) in the temperature range 6–70 K. The white solid and dashed lines in the top panels are visual aids. The solid black lines in the bottom panels are fits given by the anharmonic model, which indicates a Curie temperature (T_c) of ≈25 K. The error bars in the bottom panels represent the spectral resolution of our instrument.

which is close to the experimental value ≈25 K. We can also see that inclusion of the Hubbard-U, which accounts for Coulombic repulsion of electrons in localized Cr 3d orbitals, significantly enhances the exchange parameter J_{NN} and the Curie temperature. Thus, Cr d orbitals' Coulomb interactions are important to accurately describe $CrBr_3$.

Table 1. The exchangçe coupling, anisotropy constant, and estimated Curie temperature of monolayer $CrBr_3$ with various U_{eff}.

	$J_{NN,\,SOC}$ [meV]	D [meV]	Estimated T_c [K]
GGA	−2.46	−0.405	21.5
GGA+U (U_{eff} = 0.5 eV)	−2.64	−0.374	22.2
GGA+U (U_{eff} = 1.0 eV)	−2.79	−0.351	22.8
GGA+U (U_{eff} = 1.5 eV)	−2.95	−0.334	23.5
GGA+U (U_{eff} = 2.0 eV)	−3.10	−0.322	24.1
GGA+U (U_{eff} = 2.5 eV)	−3.23	−0.314	24.7
GGA+U (U_{eff} = 3.0 eV)	−3.35	−0.308	25.3
GGA+U (U_{eff} = 3.5 eV)	−3.48	−0.305	26.0
GGA+U (U_{eff} = 4.0 eV)	−3.60	−0.304	26.6
GGA+U (U_{eff} = 4.5 eV)	−3.72	−0.305	27.3
GGA+U (U_{eff} = 5.0 eV)	−3.84	−0.307	28.0
GGA+U (U_{eff} = 5.5 eV)	−3.95	−0.309	28.7
GGA+U (U_{eff} = 6.0 eV)	−4.06	−0.312	29.4

Next, based on the calculated exchange interactions J, we can examine the SPC effects within $CrBr_3$ with a combined DFT and finite displacement approach. Since the phonon eigenvectors are mostly unaffected by the magnetic phase transition (see Figure S3, Supporting Information, for details), only diagonal terms of the force constant matrices are changed. This approximation is reasonable if the influence of exchange interaction J is small compared to the phonon energy of the system, which is true for most phonon modes as discussed below. Based on this, and recognizing that $J(R)$ is a function of the spatial coordinates of atoms (R), we can approximate the phonon frequency shifts from the nonmagnetic to the magnetic state as

$$\Delta\omega_j = \omega_{j,\mathrm{FM}} - \omega_{j,\mathrm{NM}} \approx \frac{D_{u_j}^2\left(3J(R)|S|^2\right)}{2\omega_{j,\mathrm{FM}}} \tag{4}$$

where u is the mass-reduced phonon eigenvector for the ferromagnetic ground state, D_{u_j} is the differential operator, and $\omega_{j,\mathrm{FM}}$

is the ground state phonon frequency for phonon band index j (see Note S2, Supporting Information, for the details of derivation. Since $J(R) = \frac{E_{\mathrm{FM}} - E_{\mathrm{AFM}}}{6|S|^2}$, we obtain

$$\Delta\omega_j = \frac{D^2_{u_j}(E_{\mathrm{FM}}) - D^2_{u_j}(E_{\mathrm{AFM}})}{4\sqrt{D^2_{u_j}(E_{\mathrm{FM}})}} \tag{5}$$

and only need to calculate $D^2_{u_j}(E_{\mathrm{FM}})$ and $D^2_{u_j}(E_{\mathrm{AFM}})$ to obtain $\Delta\omega_j$. To this end, we performed finite displacement calculations with a step size 0.05 Å to obtain the second derivatives of ferromagnetic and antiferromagnetic total energies along the corresponding phonon eigenvector directions u_j. The phonon eigenvector u_j is taken from first-principle phonon calculations for ferromagnetic monolayer $\mathrm{CrBr_3}$, using the first approximation. The first-principle phonon calculation details are provided in Note S3, Supporting Information. It is worth mentioning that when $D^2_{u_j}(E_{\mathrm{FM}}) > D^2_{u_j}(E_{\mathrm{AFM}})$, the phonon modes tend to harden (phonon frequencies shift up) from the nonmagnetic to the ferromagnetic phase and vice versa.

In **Figure 4**, we show the corresponding ferromagnetic and antiferromagnetic total energies as functions of displacement from the Raman active modes. The eigenvectors of these four Raman active modes are schematically drawn in the insets of Figure 4. The phonon modes $\mathrm{A_{1g}}^1$ and $\mathrm{A_{1g}}^2$ involve Br atoms only, whereas the eigenvectors of modes $\mathrm{E_g}^2$ and $\mathrm{E_g}^3$ additionally involve small Cr contributions.

The SPC phonon shifts for monolayer $\mathrm{CrBr_3}$ in GGA+U for Hubbard-U values from 0 to 6 eV are shown in **Figure 5**a. All the phonon frequencies are blueshifted for $U_{\mathrm{eff}} > 1.0$ eV, which agrees with our experimental results. The $U_{\mathrm{eff}} = 4.5$ eV value (red circle) produces the best agreement with our experimental values (black box), as indicated in Figure 5a. We also see that for the $\mathrm{A_{1g}}^1$ mode, the calculated SPC shift deviates most from the experimental result. In Figure 4a, we see an obvious shift in the equilibrium position of phonon oscillations, as the magnetic phase transition occurs for the $\mathrm{A_{1g}}^1$ mode. This shows the corresponding phonon eigenvector is unaffected by the magnetic phase transition, which implies that our approximations are incorrect for this mode. On the other hand, there are no evident changes in the equilibrium positions of $\mathrm{E_g}^2$, $\mathrm{E_g}^3$, and $\mathrm{A_{1g}}^2$ which implies that our approximations are correct for these modes. This can be confirmed by looking at the differences between the exchange interaction J and the phonon energy. For the $\mathrm{A_{1g}}^1$ mode, the difference between J (0.15 meV) and the phonon energy (≈13.15 meV) is ≈1.14%, which is much higher than that of other modes (0.045–0.22%, see Figure S4, Supporting Information, for more details).

The U_{eff}-dependent J_{NN} and T_{c} are also calculated for the monolayer $\mathrm{CrCl_3}$ and $\mathrm{CrI_3}$, as shown in Figure 5b. For

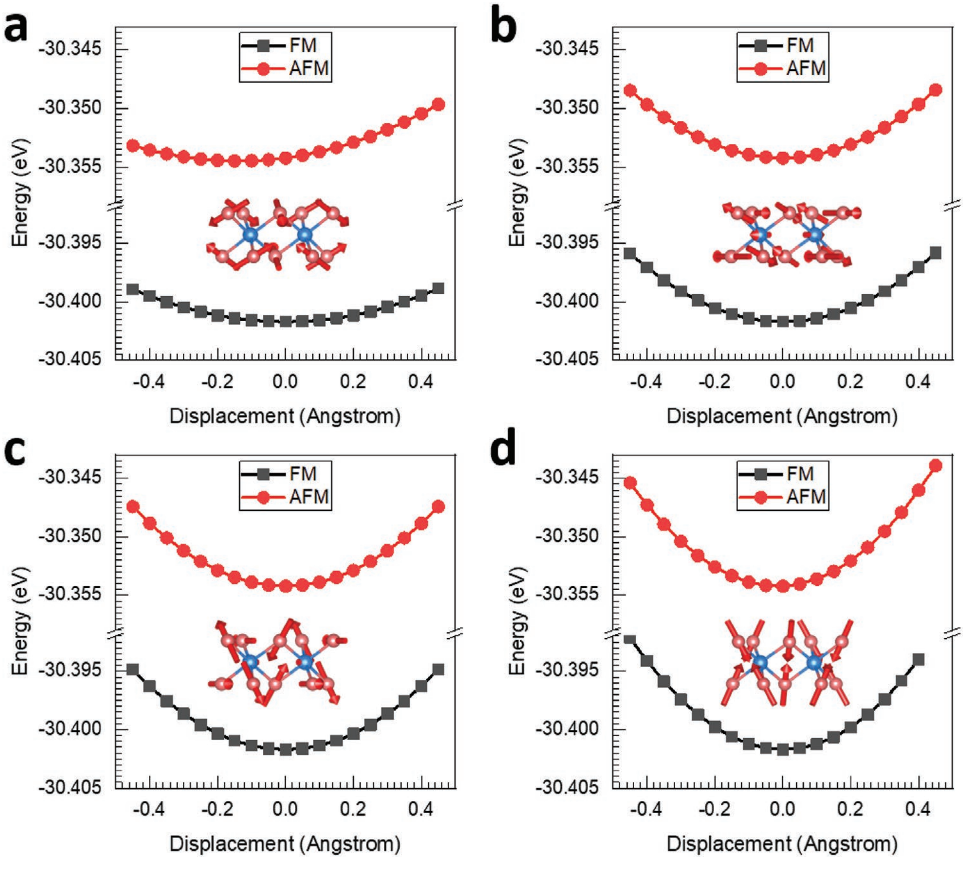

Figure 4. a–d) Calculated ferromagnetic (black circles) and antiferromagnetic (red squares) total energies with GGA+U ($U_{\mathrm{eff}} = 4.5$ eV), as a function of atomic displacements for: a) $\mathrm{A_{1g}}^1$, b) $\mathrm{E_g}^2$, c) $\mathrm{E_g}^3$, and d) $\mathrm{A_{1g}}^2$ modes. The insets show the eigenvectors of the corresponding phonon modes.

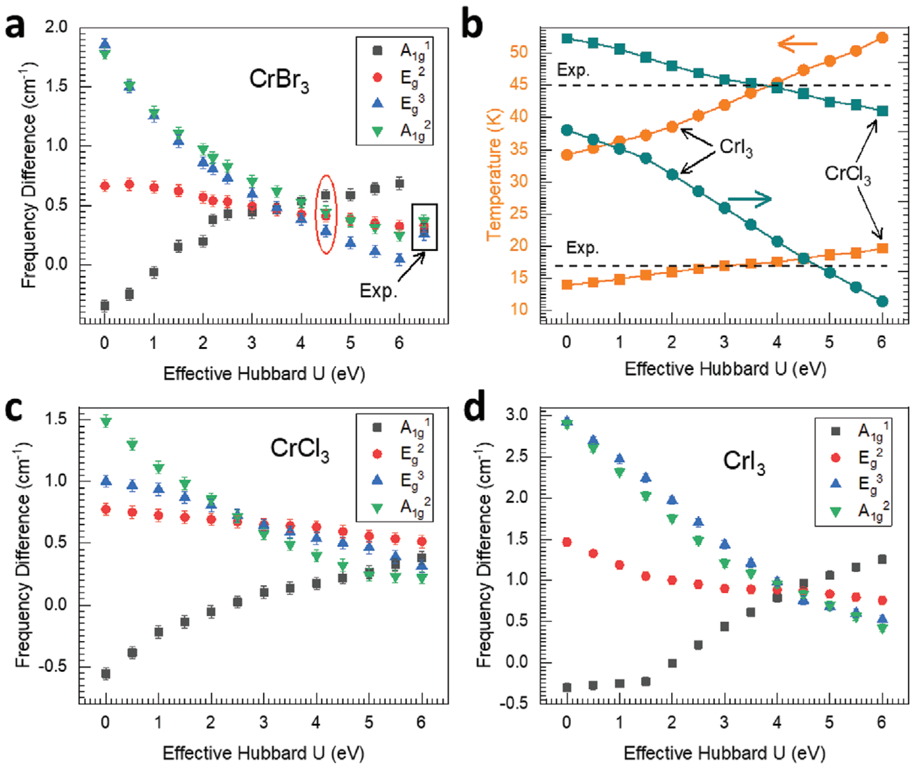

Figure 5. Calculated SPC-induced phonon shifts in monolayer a) CrBr$_3$ with various number of Effective Hubbard – U. One set of experimental values is included for comparison. b) Calculated T_c (orange dots and squares) and J_{NN} (cyan dots and squares) of CrCl$_3$ (squares) and CrI$_3$ (dots). The dashed lines show the experimental values of T_c for monolayer CrCl$_3$ and CrI$_3$. c,d) The calculated SPC-induced phonon shifts in monolayer CrCl$_3$ (c) and CrI$_3$ (d), for values of U. The error bars represent the calculations' convergence accuracy.

monolayer CrCl$_3$, when $U_{eff} = 0$, the calculated $|J_{NN}|$ ($\approx$1.66 meV) is close to the value of 1.79 meV obtained in previous works.[26] For monolayer CrI$_3$, the calculated $|J_{NN}|$ without considering U is 2.97 meV, which is also comparable to previously reported values[26] (2.71 meV). Similar to monolayer CrBr$_3$, the $|J_{NN}|$ values of both monolayer CrCl$_3$ and CrI$_3$ are proportional to U_{eff}, which indicates that T_c increases with U_{eff}. The predicted T_c values for monolayer CrCl$_3$ and CrI$_3$ are 14.0–19.7 and 34.2–52.4 K, respectively, which match well with experimentally obtained values[2,15b] of 17 and 45 K, respectively. Additionally, the SPC induced phonon shifts are also calculated for both monolayer CrCl$_3$ and CrI$_3$, with values of U_{eff} ranging from 0 to 6 eV, as shown in Figure 5c,d. Similar to monolayer CrBr$_3$, SPC-induced shifting of the A$_{1g}^1$ mode in monolayer CrCl$_3$ and CrI$_3$ increase with U_{eff}, but this has the opposite effect on the E$_g^2$, E$_g^3$, and A$_{1g}^2$ modes. When $U_{eff} > 2.0$ eV, all of the phonon frequencies are blueshifted, which indicates that SPC is highly correlated with the atomic displacement of each mode. Due to the congruency between the lattice structures of CrBr$_3$, CrCl$_3$, and CrI$_3$, the same phonon vibration modes in these three different monolayers would have similar atomic displacements. Moreover, magnetic exchange interactions play a key role in SPC. For example, at $U_{eff} = 4.5$ eV, the calculated SPC-induced shift of monolayer CrI$_3$ is around 1.0 cm^{-1}, which is higher than that of monolayer CrBr$_3$ (around 0.5 cm^{-1}) and CrCl$_3$ (average value of 0.3 cm^{-1}). This is a result of the higher J_{NN} of monolayer CrI$_3$ as compared to that of monolayer CrBr$_3$ and CrCl$_3$, as shown in Table 1 and Figure 5b.

3. Conclusion

Raman spectroscopy and first-principle calculations have been jointly utilized to study phonon properties, critical temperatures, and magnetic exchange interactions of ferromagnetic monolayer CrBr$_3$. First, the Raman active modes were identified with polarization Raman spectroscopy. A ferromagnetic transition was observed at $T_c \approx 25$ K based on phonon shifts, which is confirmed by calculating the nearest Heisenberg exchange parameter J_{NN}. Then, the SPC effect was systematically explored by using DFT and the finite-displacement approach to quantify the phonon blueshifts, which agrees with the experimental results. Specifically, the atomic-displacement-dependent J_{NN} can explain why the phonon frequency is blueshifted below T_c. We conclude that SPC is mainly caused by the changes in the exchange interactions, as the atoms oscillate about their equilibrium positions. Moreover, understanding the role of SPC effects in monolayer CrBr$_3$ paves the way to the design of 2D magnets, their heterostructures, and improving T_c, a critical design parameter.

4. Experimental Section

Sample Preparation: Bulk CrBr$_3$ was purchased from HQ Graphene. Before exfoliation, the Si/SiO$_2$ substrate was treated by ultrasonic cleaning for 10 min in acetone, isopropyl alcohol, and deionized water, and then treated by oxygen ashing. The mechanical exfoliation and atomic force microscopy measurements of the flakes were performed in a glovebox to prevent oxidation.

Raman Spectroscopy: A Jobin–Yvon HR800 system with a liquid nitrogen cooled charge-coupled detector was used to perform the Raman measurements with a back-scattering geometry. The excitation wavelength of 753 nm was from a titanium sapphire laser, and 594 nm was from a He–Ne laser. To achieve high spectral resolution (0.35 cm^{-1}), a grating with a groove density of 1800 mm^{-1} was used. A 100× objective lens with a high numerical aperture (NA = 0.9) was used to ensure a high signal-to-noise ratio. The laser power was kept low enough (<50 µW) to avoid sample heating. The sample was kept in a helium-cooled cryogenic station (Montana Instruments) while tuning the temperature between 4 and 300 K at a vacuum of 101 mbar.

Density Functional Theory Calculations: Spin-polarized density functional calculations were performed using the Vienna ab initio simulation package with projector augmented wave pseudopotentials.[28] A 450 eV energy cutoff was used for the plane wave basis set. K-points were sampled on a 13 × 13 × 1 mesh generated by the scheme of Monkhorst–Pack in the Brillouin zone. A larger than 16-Angstrom vacuum buffer was introduced between layers to avoid interlayer interactions. For obtaining the structure of monolayer $\mathrm{CrBr_3}$, we fully optimized the lattice constant, and within unit cells, the atomic positions were relaxed until the change in free energy dropped below 10^{-7} eV between two ionic steps. Tetrahedron method with Blöch corrections were used for total energy calculations. In all total energy calculations, the relaxation of the electronic degrees of freedom would be stopped if the free energy change and the band structure energy change between two steps were smaller than 10^{-8} eV. It was found that the electronic structures of Cr-trihalide were extremely sensitive to the exchange-correlation functional. It was also found, in DFT calculations, that the local-density approximation identified an antiferromagnetic phase as the ground state, which was contradictory to the experimental observations. On the other hand, the results using the GGA Perdew–Burke–Ernzerhof (GGA-PBE) agreed well with the experiment.[29] An accurate energy difference between the ferromagnetic and antiferromagnetic phases was crucial for the analysis of the SPC effect. Therefore, we only focused on the results from PBE calculations in this work. Furthermore, since pure GGA cannot correctly describe the electronic structure of strongly correlated systems, they also introduced the GGA+U[30] method in order to deal with the strong Coulomb repulsion of Cr 3d electrons. The rotationally invariant form of GGA+U[30] was applied in all total energy and phonon calculations. Effective Hubbard-U values, $U_{\mathrm{eff}} = U - J$ were used.

Supporting Information

Supporting Information is available from the Wiley Online Library or from the author.

Acknowledgements

J.W., Y.Y., and M.-L.L. contributed equally to this work. S.H. would like to acknowledge the support by the US Department of Energy under grant number DE-FG02-05ER46240. The numerical computations were carried out on the University of Southern California High Performance Supercomputer Cluster. M.R. would like to acknowledge the Alexander von Humboldt Foundation for support. The authors would like to thank Max R. Lien for the useful discussion.

Conflict of Interest

The authors declare the following competing interests: H.W. currently also has an appointment with Taiwan Semiconductor Manufacturing Company (TSMC).

Data Availability Statement

The data that support the findings of this study are available from the corresponding author upon reasonable request.

Keywords

chromium tribromide, Curie temperature, phonon shifts, spin–phonon coupling, 2D magnets

Received: October 23, 2021
Revised: March 7, 2022

---

[1] C. Gong, L. Li, Z. Li, H. Ji, A. Stern, Y. Xia, T. Cao, W. Bao, C. Wang, Y. Wang, *Nature* **2017**, *546*, 265.

[2] B. Huang, G. Clark, E. Navarro-Moratalla, D. R. Klein, R. Cheng, K. L. Seyler, D. Zhong, E. Schmidgall, M. A. McGuire, D. H. Cobden, *Nature* **2017**, *546*, 270.

[3] a) D. Ghazaryan, M. T. Greenaway, Z. Wang, V. H. Guarochico-Moreira, I. J. Vera-Marun, J. Yin, Y. Liao, S. V. Morozov, O. Kristanovski, A. I. Lichtenstein, M. I. Katsnelson, F. Withers, A. Mishchenko, L. Eaves, A. K. Geim, K. S. Novoselov, A. Misra, *Nat. Electron.* **2018**, *1*, 344; b) W. Chen, Z. Sun, Z. Wang, L. Gu, X. Xu, S. Wu, C. Gao, *Science* **2019**, *366*, 983.

[4] a) Y. Deng, Y. Yu, Y. Song, J. Zhang, N. Z. Wang, Z. Sun, Y. Yi, Y. Z. Wu, S. Wu, J. Zhu, *Nature* **2018**, *563*, 94; b) Z. Fei, B. Huang, P. Malinowski, W. Wang, T. Song, J. Sanchez, W. Yao, D. Xiao, X. Zhu, A. F. May, *Nat. Mater.* **2018**, *17*, 778.

[5] a) T. Li, S. Jiang, N. Sivadas, Z. Wang, Y. Xu, D. Weber, J. E. Goldberger, K. Watanabe, T. Taniguchi, C. J. Fennie, *Nat. Mater.* **2019**, *18*, 1303; b) S. Jiang, L. Li, Z. Wang, K. F. Mak, J. Shan, *Nat. Nanotechnol.* **2018**, *13*, 549; c) T. Song, Z. Fei, M. Yankowitz, Z. Lin, Q. Jiang, K. Hwangbo, Q. Zhang, B. Sun, T. Taniguchi, K. Watanabe, M. McGuire, D. Graf, T. Cao, J. Chu, D. H. Cobden, C. R. Dean, D. Xiao, X. Xu, *Nat. Mater.* **2019**, *18*, 1302; d) B. Huang, G. Clark, D. R. Klein, D. MacNeill, E. Navarro-Moratalla, K. L. Seyler, N. Wilson, M. A. McGuire, D. H. Cobden, D. Xiao, *Nat. Nanotechnol.* **2018**, *13*, 544; e) S. Jiang, J. Shan, K. F. Mak, *Nat. Mater.* **2018**, *17*, 406.

[6] a) S. Jiang, L. Li, Z. Wang, J. Shan, K. F. Mak, *Nat. Electron.* **2019**, *2*, 159; b) T. Song, X. Cai, M. W.-Y. Tu, X. Zhang, B. Huang, N. P. Wilson, K. L. Seyler, L. Zhu, T. Taniguchi, K. Watanabe, *Science* **2018**, *360*, 1214; c) T. Song, M. W.-Y. Tu, C. Carnahan, X. Cai, T. Taniguchi, K. Watanabe, M. A. McGuire, D. H. Cobden, D. Xiao, W. Yao, *Nano Lett.* **2019**, *19*, 915.

[7] a) J.-H. Park, Y. Kim, W. C. Lim, J. H. Kim, S. H. Park, J. H. Kim, W. Kim, K. W. Kim, J. H. Jeong, K. S. Kim, H. Kim, Y. J. Lee, S. C. Og, J. E. Lee, S. O. Park, S. Watts, D. Apalkov, V. Nikitin, M. Krounbi, S. Jeong, S. Choi, K. Kang, C. Chung, in *2012 Symp. on VLSI Technology (VLSIT)*, IEEE, Piscataway, NJ, USA, **2012**, pp. 57–58; b) D. L. Cortie, G. L. Causer, K. C. Rule, H. Fritzsche, W. Kreuzpaintner, F. Klose, *Adv. Funct. Mater.* **2020**, *30*, 1901414.

[8] a) J. H. Lee, K. M. Rabe, *Phys. Rev. B* **2011**, *84*, 104440; b) A. Kumar, C. Fennie, K. Rabe, *Phys. Rev. B* **2012**, *86*, 184429; c) C. Kant, J. Deisenhofer, T. Rudolf, F. Mayr, F. Schrettle, A. Loidl, V. Gnezdilov, D. Wulferding, P. Lemmens, V. Tsurkan, *Phys. Rev. B* **2009**, *80*, 214417; d) M. Iliev, H. Guo, A. Gupta, *Appl. Phys. Lett.* **2007**, *90*, 151914; e) C. J. Fennie, K. M. Rabe, *Phys. Rev. Lett.* **2006**, *96*, 205505; f) L. Casto, A. Clune, M. Yokosuk, J. Musfeldt, T. Williams, H. Zhuang, M.-W. Lin, K. Xiao, R. Hennig, B. Sales, *APL Mater.* **2015**, *3*, 041515; g) E. Aytan, B. Debnath, F. Kargar, Y. Barlas, M. Lacerda, J. Li, R. Lake, J. Shi, A. Balandin, *Appl. Phys. Lett.* **2017**, *111*, 252402; h) B. Zhang, Y. Hou, Z. Wang, R. Wu, *Phys. Rev. B* **2019**, *100*, 224427.

[9] a) M. Testa-Anta, M. A. Ramos-Docampo, M. Comesaña-Hermo, B. Rivas-Murias, V. Salgueiriño, *Nanoscale Adv.* **2019**, *1*, 2086; b) X. Zhang, X.-F. Qiao, W. Shi, J.-B. Wu, D.-S. Jiang, P.-H. Tan,

Chem. Soc. Rev. **2015**, *44*, 2757; c) J.-B. Wu, M.-L. Lin, X. Cong, H.-N. Liu, P.-H. Tan, *Chem. Soc. Rev.* **2018**, *47*, 1822; d) J. Wu, X. Cong, S. Niu, F. Liu, H. Zhao, Z. Du, J. Ravichandran, P. H. Tan, H. Wang, *Adv. Mater.* **2019**, *31*, 1902118.

[10] a) X. Wang, K. Du, Y. Y. F. Liu, P. Hu, J. Zhang, Q. Zhang, M. H. S. Owen, X. Lu, C. K. Gan, P. Sengupta, *2D Mater.* **2016**, *3*, 031009; b) Y. Tian, M. J. Gray, H. Ji, R. J. Cava, K. S. Burch, *2D Mater.* **2016**, *3*, 025035; c) K. Kim, S. Y. Lim, J.-U. Lee, S. Lee, T. Y. Kim, K. Park, G. S. Jeon, C.-H. Park, J.-G. Park, H. Cheong, *Nat. Commun.* **2019**, *10*, 1784; d) D. Lockwood, M. Cottam, *J. Appl. Phys.* **1988**, *64*, 5876.

[11] L. Woods, *Phys. Rev. B* **2001**, *65*, 014409.

[12] K. Sinha, U. Upadhyaya, *Phys. Rev.* **1962**, *127*, 432.

[13] L. Webster, L. Liang, J.-A. Yan, *Phys. Chem. Chem. Phys.* **2018**, *20*, 23546.

[14] K. L. Seyler, D. Zhong, D. R. Klein, S. Gao, X. Zhang, B. Huang, E. Navarro-Moratalla, L. Yang, D. H. Cobden, M. A. McGuire, *Nat. Phys.* **2018**, *14*, 277.

[15] a) Z. Zhang, J. Shang, C. Jiang, A. Rasmita, W. Gao, T. Yu, *Nano Lett.* **2019**, *19*, 3138; b) H. H. Kim, B. Yang, S. Li, S. Jiang, C. Jin, Z. Tao, G. Nichols, F. Sfigakis, S. Zhong, C. Li, *Proc. Natl. Acad. Sci. USA* **2019**, *116*, 11131.

[16] Y. Zhang, X. Wu, B. Lyu, M. Wu, S. Zhao, J. Chen, M. Jia, C. Zhang, L. Wang, X. Wang, *Nano Lett.* **2019**, *20*, 729.

[17] a) J.-B. Wu, X. Zhang, M. Ijäs, W.-P. Han, X.-F. Qiao, X.-L. Li, D.-S. Jiang, A. C. Ferrari, P.-H. Tan, *Nat. Commun.* **2014**, *5*, 5309; b) J.-B. Wu, Z.-X. Hu, X. Zhang, W.-P. Han, Y. Lu, W. Shi, X.-F. Qiao, M. Ijiäs, S. Milana, W. Ji, *ACS Nano* **2015**, *9*, 7440.

[18] M. Balkanski, R. Wallis, E. Haro, *Phys. Rev. B* **1983**, *28*, 1928.

[19] a) T. Yin, K. A. Ulman, S. Liu, A. G. del Águila, Y. Huang, L. Zhang, M. Serra, D. Sedmidubsky, Z. Sofer, S. Y. Quek, *Adv. Mater.* **2021**, *33*, 2101618; b) D. Kozlenko, O. Lis, S. Kichanov, E. Lukin, N. Belozerova, B. Savenko, *npj Quantum Mater.* **2021**, *6*, 19.

[20] M. Kim, P. Kumaravadivel, J. Birkbeck, W. Kuang, S. G. Xu, D. Hopkinson, J. Knolle, P. A. McClarty, A. Berdyugin, M. B. Shalom, *Nat. Electron.* **2019**, *2*, 457.

[21] W. Geertsma, D. Khomskii, *Phys. Rev. B* **1996**, *54*, 3011.

[22] J. L. Lado, J. Fernández-Rossier, *2D Mater.* **2017**, *4*, 035002.

[23] O. Besbes, S. Nikolaev, N. Meskini, I. Solovyev, *Phys. Rev. B* **2019**, *99*, 104432.

[24] I. Kashin, V. Mazurenko, M. Katsnelson, A. Rudenko, *2D Mater.* **2020**, *7*, 025036.

[25] a) A. E. Shields, D. Santos-Carballal, N. H. de Leeuw, *J. Nucl. Mater.* **2016**, *473*, 99; b) T. Wang, N. Qiu, X. Wen, Y. Tian, J. He, K. Luo, X. Zha, Y. Zhou, Q. Huang, J. Lang, *J. Nucl. Mater.* **2016**, *469*, 194.

[26] W.-B. Zhang, Q. Qu, P. Zhu, C.-H. Lam, *J. Mater. Chem. C* **2015**, *3*, 12457.

[27] D. Torelli, T. Olsen, *2D Mater.* **2018**, *6*, 015028.

[28] a) G. Kresse, D. Joubert, *Phys. Rev. B* **1999**, *59*, 1758; b) G. Kresse, J. Furthmüller, *Phys. Rev. B* **1996**, *54*, 11169.

[29] J. P. Perdew, K. Burke, M. Ernzerhof, *Phys. Rev. Lett.* **1996**, *77*, 3865.

[30] A. Liechtenstein, V. Anisimov, J. Zaanen, *Phys. Rev. B* **1995**, *52*, R5467.